13th ewtec 2019 Proceedings of the 13th European Wave and Tidal Energy Conference 1-6 Sept 2019, Naples, Italy

CCP-WSI Blind Test Series 2: A Nonlinear Froude-Krylov Modelling Approach

Giuseppe Giorgi

Abstract—**The accuracy of mathematical models strongly influences the design and effectiveness of wave energy converters, and hence the ability to achieve economic viability and industrial feasibility. Despite the fact that the wave energy field is at least 45 years old, there is still a clear lack of standardization of modelling techniques, and a need for increasing confidence in hydrodynamic models. The Collaborative Computational Project in Wave Structure Interaction (CCP-WSI) aims to define a level playing field of comparison for a plurality of models, evaluating their performance using clearly pre-defined metrics. This paper implements a computationally convenient approach to represent nonlinear Froude-Krylov forces, along with the inclusion of nonlinear kinematics. The objective is to define a medium-high fidelity model that is able to compute at a fraction of the computational time typically required by fully-nonlinear models. Three focused waves are used as a case study, representative of highly-nonlinear sea states, hence particularly challenging to be modelled using partially-nonlinear potential theory-based mathematical models. Details and a critical discussion about the implementation are provided. A small computational time is obtained (between 4 and 13 times the simulation time). Results show major nonlinear effects, such as drift and nonlinear coupling between different degrees of freedom.**

Index Terms—**Nonlinear Froude-Krylov force, CCP-WSI blind tests, wave energy converters, focused waves.**

I. Introduction

THE present renewable energy market is so competitive that wave energy converter (WEC) developers are under pressure to reduce the cost of energy and achieve economic viability. One major obstacle present in wave energy applications is the rather low level of confidence developers have in their mathematical models. The performance of a WEC energy conversion and control strategy strongly depends on the representativeness of the model [1], [2]. Moreover, it is critical to rely on a trustworthy prediction of structural loads to ensure safety of personnel and/or components, while avoiding over-sizing of the structure and excessive safety coefficients.

Although the "modelling problem" of wave energy converters (WECs) is at least 45 years old [3], it is still far from being settled. Early (linear) WEC models, naturally germinated from classic ocean engineering, are usually not fit to accurately describe the wave energy problem, since the objective of WECs is to exaggerate their motion and maximise power absorption (as opposed to motion stabilization). However, the inclusion of nonlinearities, essential for achieving higher accuracy, also requires an increase in model complexity, and therefore computational burden. In the pursuit of the best compromise between model fidelity and computational time, a large number of nonlinear models have appeared in recent years [4]. The performance of each model strongly depends on the specific device shape [5], dimension [6], installation site [7], conversion principle [8], and operational condition [9]. Furthermore, there are different accuracy/computational requirements according to the model's purpose (i.e. design, model-based control, simulation, survivability, etc.). Therefore, although comparison between different modelling approaches is a challenging task, recent years have witnessed the pressing need for consistent model evaluation and standardization [10]. A shared effort from several players in the wave energy community lead to a modelling competition [11], the IEA-OES project [12], and, finally, the present CCP-WSI project, which this work is part of.

The objective of the CCP-WSI (Collaborative Computational Project in Wave Structure Interaction) project is to define a level playing field of comparison, with clear evaluation metrics, supported by experimental data. However, as in the previous version in [13], the participants have no access to these data (blind-test), so tuning the model based on the expected results is not possible. The modelling approach proposed in this paper is based on partially-nonlinear potential theory, with the inclusion of nonlinear kinematics [14] and analytical nonlinear Froude-Krylov (FK) forces [15]. Such a model purports to achieve a higher level of accuracy (compared to a fully-linear model) at a small fraction of the computational time required by fully-nonlinear models.

II. Equation of Motion

In order to conveniently describe wave-structure interactions and the floater kinematics and dynamics, let us define two different frames of reference, as shown in Fig. 1. The first one is an inertial frame (x, y, z), with x along and concordant with the positive wave propagation direction, z vertical and positive upwards, y according to the right-hand rule, and the origin at the centroid of the water plane area of the floater in static equilibrium. Since its directions are constant in time, this frame is best used to keep track of the floater *displacement* $\boldsymbol{\zeta}$:

$$\boldsymbol{\zeta} = \begin{bmatrix} \mathbf{p} \\ \boldsymbol{\Theta} \end{bmatrix} \tag{1a}$$

Paper ID: 1274, Track: Wave Hydrodynamic Modelling.
Giuseppe Giorgi is with the Department of Mechanics and Aerospace Engineering, Politecnico di Torino, Turin, Italy (giuseppe.giorgi@polito.it).

$$\mathbf{p} = \begin{bmatrix} x \\ y \\ z \end{bmatrix} \tag{1b}$$

$$\boldsymbol{\Theta} = \begin{bmatrix} \phi \\ \theta \\ \psi \end{bmatrix} \tag{1c}$$

where $\mathbf{p}$ represents linear positions (surge, sway, and heave), and $\boldsymbol{\Theta}$ represents angular positions (roll, pitch, and yaw). However, it is convenient to formulate the dynamic equation of motion in a body-fixed frame $(\hat{x}, \hat{y}, \hat{z})$, so that moments of inertia are time-invariant. Furthermore, if the centre of gravity (CoG) is chosen as the origin of the body-fixed frame, such moments of inertia are minimal and the inertia matrix is diagonal.

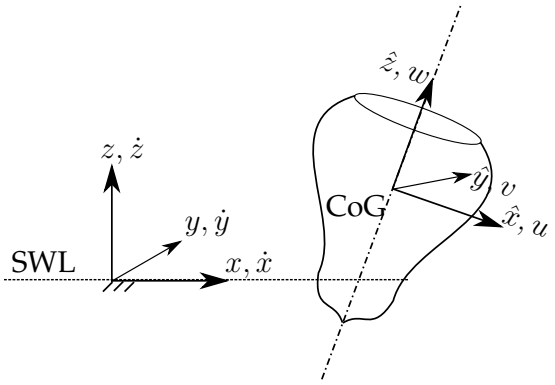

Fig. 1. Inertial frame (x, y, z), with the origin at still water level (SWL), and body-fixed (non-inertial) frame $(\hat{x}, \hat{y}, \hat{z})$, with the origin at the centre of gravity (CoG) of the body. Velocities according to the inertial frame $(\dot{x}, \dot{y}, \dot{z})$ and the body-fixed frame (u, v, w)

However, since the body-fixed frame is rotating (hence accelerating) with the body, non-inertial effects should be taken into account, namely Coriolis and centripetal forces. Newton's equation of motion is defined according to the floater *velocity* $\boldsymbol{\nu}$, expressed in the body-fixed frame:

$$\boldsymbol{\nu} = \begin{bmatrix} \mathbf{v} \\ \boldsymbol{\omega} \end{bmatrix} \tag{2a}$$

$$\nu = \begin{bmatrix} u \\ v \\ w \end{bmatrix} \tag{2b}$$

$$\boldsymbol{\omega} = \begin{bmatrix} p \\ q \\ r \end{bmatrix} \tag{2c}$$

where ν represents linear velocities and $\boldsymbol{\omega}$ represents angular velocities.

The rate of change of displacements in the global frame ($\dot{\boldsymbol{\zeta}}$) is computed from the body velocities ($\boldsymbol{\nu}$) by means a transformation matrix ($\mathbf{J}_{\boldsymbol{\Theta}}$), depending on the instantaneous angular orientation of the body-fixed frame with respect to the inertial frame ($\boldsymbol{\Theta}$). Please refer to Sect. II-A for further details. Therefore, displacement and velocity of the body are computed by solving the following set of first-order differential equations:

$$\begin{cases} \dot{\boldsymbol{\zeta}} = \mathbf{J}_{\boldsymbol{\Theta}} \boldsymbol{\nu} \\ \mathbf{M}\dot{\boldsymbol{\nu}} + \mathbf{C}_{Cor}\boldsymbol{\nu} = \mathbf{F}_d + \mathbf{F}_{FK} + \mathbf{F}_{rad} + \mathbf{F}_{moor}, \end{cases} \tag{3}$$

where $\mathbf{M}$ is the inertial matrix, $\mathbf{F}_{Cor} = \mathbf{C}_{Cor}\boldsymbol{\nu}$ is the Coriolis/centripetal force, $\mathbf{F}_d$ is the linear diffraction force, $\mathbf{F}_{rad}$ is the radiation force, and $\mathbf{F}_{moor}$ is the mooring force. Note that $\mathbf{F} \in \mathbb{R}^6$ is a generalized force, composed of a linear force vector $\mathbf{f} \in \mathbb{R}^3$, and a torque vector $\boldsymbol{\tau} \in \mathbb{R}^3$.

Considering the body to be small compared to the typical wavelength, it is reasonable to assume linear diffraction and radiation forces [6]. Furthermore, by means of a moment-matching identification technique it is possible to replace the radiation convolution integral by a computationally convenient state space [16]. On the other hand, since large motions are expected from a wave energy converter in order to maximize power absorption, the following nonlinearities should be considered:

- nonlinear kinematics, due to large rotational displacements and velocities (see Sect. II-A);
- nonlinear FK forces, due to large translational and rotational displacements, making variations of the instantaneous wetted surface significant (see Sect. II-B).

A. Nonlinear kinematics

Let us define, for convenience of notation, the skew-symmetric operator $\mathcal{S} : \mathbb{R}^3 \to \mathbb{R}^{3\times3}$ as

$$\mathcal{S} : \left\{ \boldsymbol{\lambda} \in \mathbb{R}^3 \,\middle|\, \mathcal{S}(\boldsymbol{\lambda}) \triangleq \begin{bmatrix} 0 & -\lambda_3 & \lambda_2 \\ \lambda_3 & 0 & -\lambda_1 \\ -\lambda_2 & \lambda_1 & 0 \end{bmatrix} \right\}. \tag{4}$$

It follows that $\mathcal{S}(\boldsymbol{\lambda}) = -\mathcal{S}(\boldsymbol{\lambda})^T$, and that the cross-product can be written as:

$$\boldsymbol{\lambda} \times \mathbf{a} = \mathcal{S}(\boldsymbol{\lambda})\mathbf{a} \tag{5}$$

Since the equation of motion is described in a rotating (hence accelerating) frame of reference, Coriolis and centripetal effects should be taken into account. When defined about the CoG, these are computed as follows [14]:

$$\mathbf{F}_{Cor} = \mathbf{C}_{Cor}\boldsymbol{\nu} = \begin{bmatrix} m\mathcal{S}(\boldsymbol{\omega}) & \mathbf{0}_{3\times3} \\ \mathbf{0}_{3\times3} & -\mathcal{S}(\mathbf{I}_g\boldsymbol{\omega}) \end{bmatrix} \begin{bmatrix} \mathbf{v} \\ \boldsymbol{\omega} \end{bmatrix}, \tag{6}$$

where m is the mass of the body, and $\mathbf{I}_g$ is the matrix of the moments of inertia with respect to CoG.

Instantaneous velocities generate infinitesimal displacements along the body-fixed axis, which are continuously changing direction in time. Therefore, it is necessary to determine the rate of change of the displacements ($\dot{\boldsymbol{\zeta}}$) in the global coordinate system by applying the following instantaneous rotations to $\boldsymbol{\nu}$:

$$\dot{\boldsymbol{\zeta}} = \begin{bmatrix} \dot{\mathbf{p}} \\ \dot{\boldsymbol{\Theta}} \end{bmatrix} = \begin{bmatrix} \mathbf{R}_{\boldsymbol{\Theta}} & \mathbf{0}_{3\times3} \\ \mathbf{0}_{3\times3} & \mathbf{T}_{\boldsymbol{\Theta}} \end{bmatrix} \begin{bmatrix} \mathbf{v} \\ \boldsymbol{\omega} \end{bmatrix} = \mathbf{J}_{\boldsymbol{\Theta}}\boldsymbol{\nu}, \tag{7}$$

where $\mathbf{R}_{\boldsymbol{\Theta}}$ is the rotation matrix, depending on the Euler angles $\boldsymbol{\Theta}$, defined according to the 3-2-1 convention as:

$$\begin{aligned} \mathbf{R}_{\boldsymbol{\Theta}} &= \mathbf{R}_{\hat{z},\psi}\mathbf{R}_{\hat{y},\theta}\mathbf{R}_{\hat{x},\phi} \\ &= \begin{bmatrix} c\psi & -s\psi & 0 \\ s\psi & c\psi & 0 \\ 0 & 0 & 1 \end{bmatrix} \begin{bmatrix} c\theta & 0 & s\theta \\ 0 & 1 & 0 \\ -s\theta & 0 & c\theta \end{bmatrix} \begin{bmatrix} 1 & 0 & 0 \\ 0 & c\phi & -s\phi \\ 0 & s\phi & c\phi \end{bmatrix}, \end{aligned} \tag{8}$$

with c and s standing for $\cos()$ and $\sin()$ trigonometric operators, respectively. $\mathbf{R}_{\boldsymbol{\Theta}}$ is applied to translational velocities, and $\mathbf{T}_{\boldsymbol{\Theta}}$ is applied to rotational ones and is defined as follows:

$$\mathbf{T}_{\boldsymbol{\Theta}} = \begin{bmatrix} 1 & s\phi \cdot t\theta & c\phi \cdot t\theta \\ 0 & c\phi & -s\phi \\ 0 & s\phi/c\theta & c\phi/c\theta \end{bmatrix}, \tag{9}$$

where t stands for the $\tan()$ trigonometric operator. Note that the singularity of $\mathbf{T}_{\boldsymbol{\Theta}}$ in $\pm\pi/2$ is usually not an issue in wave energy applications, since the amplitude of the pitch angle is, by design, always expected to be smaller than $\pi/2$.

Note that, if small angular velocities and displacement are assumed (as in the usual linear approximation), Coriolis-centripetal forces in (6) are negligible, and $\mathbf{J}_{\boldsymbol{\Theta}}$ in (7) becomes the identity matrix. Consequently, displacement according to inertial and non-inertial frames are equivalent [14]. However, in this paper such an approximation is rejected, since large pitch angles are expected.

B. Nonlinear Froude-Krylov force

Froude-Krylov forces are defined as the integral of the undisturbed pressure field (p) over the wetted surface of the floater. In the linear approximation, it is assumed that the relative motion between the body and the free surface is small, so that FK forces are computed with respect to the mean wetted surface. On the contrary, nonlinear FK force calculations are performed with respect to the actual *instantaneous* wetted surface ($S_w(t)$):

$$\mathbf{f}_{FK} = \mathbf{f}_g + \iint_{S_w(t)} p\mathbf{n}\, dS, \tag{10a}$$

$$\boldsymbol{\tau}_{FK} = \mathbf{r}_g \times \mathbf{f}_g + \iint_{S_w(t)} p\mathbf{r} \times \mathbf{n}\, dS, \tag{10b}$$

where $\mathbf{f}_g$ is the gravity force, $\mathbf{n}$ is the unity vector normal to the surface, $\mathbf{r}$ is the generic position vector, and $\mathbf{r}_g$ is the position vector of the CoG. The undisturbed incident pressure field of uni-directional regular wave is defined as:

$$p(x,z,t) = -\rho g z + a\cos(\omega t - kx)\,\frac{\cosh(k(z'+h))}{\cosh(kh)}, \tag{11}$$

where a, ω, and k are the wave amplitude, frequency, and number, respectively, ρ the water density, g the acceleration of gravity, h the water depth, and z' the vertical coordinate modified according to Wheeler's stretching [7]. Stretching techniques are a pragmatic way to amend to violations of the free surface boundary conditions of linear potential flow approaches. Although, when used for NLFK calculations, they always improve Airy's theory results [7], their accuracy in describing the pressure field decays with the degree of nonlinearity of the wave, namely with its steepness. Hence, it is reasonable to expect that the actual pressure field of the particularly steep focused waves considered in this study would differ. A comparison with experiments or CFD simulations would be useful to quantify such a difference.

Solving integrals in (10) requires, in general, computationally demanding mesh-based approaches [17]. However, computationally efficient approaches are available for axisymmetric bodies [15], exploiting cylindrical coordinates (ϱ,ϑ) to achieve an analytical representation of the wetted surface:

$$\begin{cases} \hat{x}(\varrho,\vartheta) = f(\varrho)\cos\vartheta \\ \hat{y}(\varrho,\vartheta) = f(\varrho)\sin\vartheta \\ \hat{z}(\varrho,\vartheta) = \varrho \end{cases} \quad , \quad \vartheta \in [-\pi,\pi) \wedge \varrho \in [\varrho_1,\varrho_2] \tag{12}$$

where $f(\varrho)$ is a generic function of the vertical coordinate ϱ, describing the profile of revolution of the axisymmetric body. Since it is convenient to define the FK integrals in the body-fixed frame of reference, the pressure field must be mapped from the inertial to the body-fixed frame. Therefore, after some manipulations [18], the integral in (10a), for example, becomes:

$$\begin{aligned} \mathbf{f}_{FK} &= \mathbf{R}_{\boldsymbol{\Theta}}^T\mathbf{f}_g + \iint_{S_w(t)} p(\hat{x},\hat{y},\hat{z})\mathbf{n}dS = \\ &= \mathbf{R}_{\boldsymbol{\Theta}}^T\mathbf{f}_g + \int_{-\pi}^{\pi}\int_{\varrho_1}^{\varrho_2} p(\varrho,\vartheta)\mathbf{e}_\varrho \times \mathbf{e}_\vartheta d\varrho d\vartheta, \end{aligned} \tag{13}$$

where $\mathbf{e}_\varrho$ and $\mathbf{e}_\vartheta$ are the unity vector along ϱ and ϑ, respectively. Note that the transpose of rotation matrix is used to map the gravity force in the body-fixed frame. The integral in (13) is solved numerically, using a 2D-quadrature scheme for trapezoidal integration.

III. Wave tank experiments

The focus of the CCP-WSI Blind Test Series 2 is to study hydrodynamic interactions between small bodies and large, steep waves, in order to be representative of point-absorbing WECs in harsh sea states, at the boundary of the power production region. In order to replicate extreme wave conditions, focused waves are considered, which are created applying the NewWave

TABLE I
BLIND TEST 2 (BT2) INCIDENT WAVE IDENTIFICATION NUMBER (ID), AMPLITUDE (A), PEAK FREQUENCY (f_p), SIGNIFICANT WAVE HEIGHT OF THE ORIGINAL PIERSON-MOSKOWITZ SPECTRUM (H_s), AND WAVE STEEPNESS (kA).

ID	A [m]	f_p [Hz]	H_s [m]	kA
1BT2	0.25	0.3578	3.0	0.128778
2BT2	0.25	0.4000	3.0	0.160972
3BT2	0.25	0.4382	3.0	0.193167

theory [19] to a Pierson-Moskowitz spectrum (significant wave height H_s), so that all frequency components arrive with zero phase angle at the focus location, where the device is placed. Three waves are considered, with the same amplitude (A) but increasing peak frequency (f_p), hence steepness (kA), which is an indicator of nonlinearity. Table I tabulates waves characteristics and identification codes (ID), while Fig. 2 shows the time traces, only in the time window considered for the comparison, between 35.3s and 50.3s. In the simulations performed for this work, the components of the free surface elevation have been reconstructed from data collected by wave gauges in the wave tank, applying a fast-Fourier transform to filtered and windowed data, and applying a cut-off frequency of 14 rad·s^{-1}.

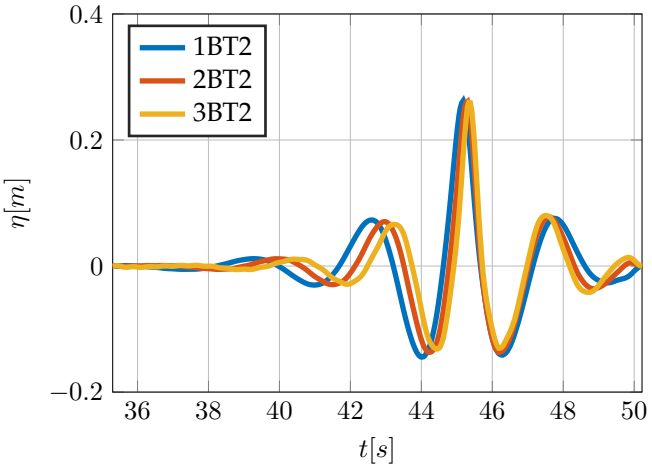

Fig. 2. Incident free surface elevation in the time window considered for the analysis.

Two surface-piercing structures have been considered, whose shape and dimensions, compared to the wave length, are characteristic of typical wave energy converters. Two geometries are considered: one hemispherical-bottomed cylinder (G_1), and a cylinder with a moon-pool (G_2). Figure 3 shows the cross-sections of the two geometries, along with dimensions (in mm) and position with respect to the still water level (SWL). Table II tabulates the mass and moments of inertia of the two bodies. Dimensions and inertial properties are out-of-date for the purposes of the CCP-WSI-BT2 comparison. Both floaters are moored to the tank floor (water depth 3m) by means of a single pre-tensioned mooring line.

The mooring system is composed of a single line, anchored at the tank floor and attached at the bottom of

TABLE II
MASS AND INERTIA OF THE TWO FLOATERS

	$M[kg]$	$I_{xx}[kgm^2]$	$I_{yy}[kgm^2]$	$I_{zz}[kgm^2]$
G_1	43.674	2.219	2.219	1.143
G_2	61.459	1.790	1.790	3.298

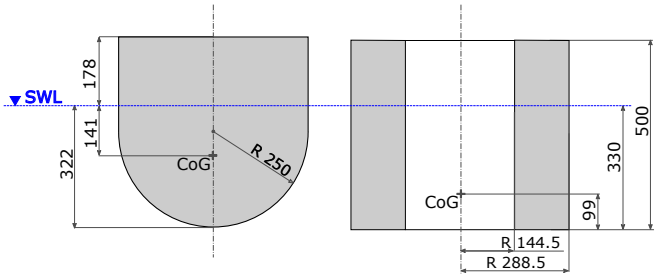

Fig. 3. Dimensions and position (in mm) with respect to the still water level (SWL) of the cross-section of geometry G_1, at the left, and G_2, at the right.

the device, as shown in Fig. 4. The axial stiffness K_{moor} is the same for both geometries, and equal to 67Nm; the rest length (L_0) is 2.211m for G_1, and 2.204m for G_2. Thanks to the universal joint connecting the mooring line to the floater, $\mathbf{f}_{moor}$ is generally not aligned to the buoy axis, hence $\boldsymbol{\tau}_{moor}$ is not zero. Therefore, the mooring force is computed, in the body-fixed frame, as follows:

$$\mathbf{F}_{moor} = \begin{bmatrix} \mathbf{f}_{moor} \\ \boldsymbol{\tau}_{moor} \end{bmatrix} = \begin{bmatrix} \mathbf{e}_m K_{moor} \Delta L \\ \mathbf{r}_b \times \mathbf{f}_{moor} \end{bmatrix} \tag{14}$$

where $\mathbf{e}_m$ is the unit vector of the mooring line and $\mathbf{r}_b$ is the position of the attach point of the mooring line at the bottom of the floater, both defined with respect to the body-fixed frame.

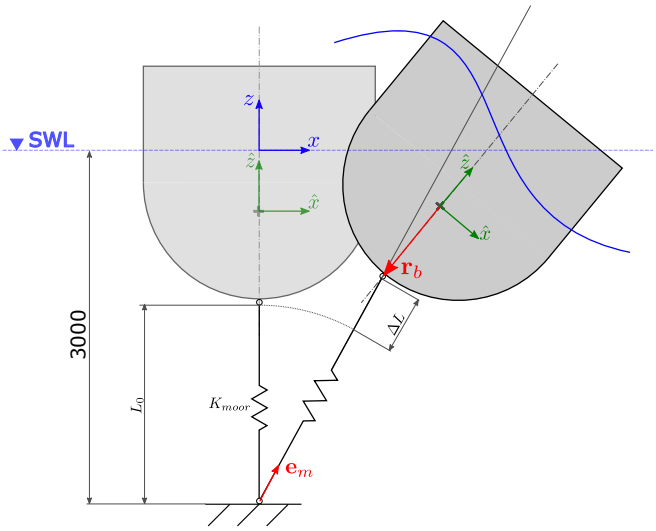

Fig. 4. Global and body-fixed frames of reference, shown at the static equilibrium (left) and in operation (right). Schematics of the mooring system, with initial length (L_0) and axial stiffness (K_{moor}) defining the pretension, and line extension ΔL. $\mathbf{e}_m$ is the unit vector of the mooring line and $\mathbf{r}_b$ is the position of the attach point of the mooring line at the bottom of the floater. Water depth shown in mm.

IV. Results

In order to verify the correctness of the implementation and to validate the modelling approach, it is useful to compute the response amplitude operator (RAO) in both the frequency and the time domain, defined as the complex ratio between the response and the incoming wave. The boundary element method (BEM) software, Wamit, is used to compute the hydrodynamic coefficients in the frequency domain. A second-order Runge-Kutta integration scheme is used to compute the solution in the time domain. While the frequency domain approach requires a linear formulation, nonlinearities can be included in the time domain. Both a fully-linear and the nonlinear model have been used for building the RAO in the time domain. However, linear conditions have been considered (linear moorings and very small waves, with 1mm wave height), so that the frequency approach and the two time domain approaches must overlap. Figures 5 and 6 show this overlap for geometries G_1 and G_2, respectively.

The constant time step used for the Runge-Kutta integration scheme is defined through a convergence study, in order to achieve a satisfactory compromise between accuracy and computational time. Considering, for example, the response of geometry G_1 to the harsher wave 3BT2, Fig. 7 shows the relative computational time (t_r) and the percentage error (ε) depending on the time step dt, where ϵ is defined as:

$$\varepsilon = mean\left(rms\left(\frac{|\boldsymbol{\zeta} - \boldsymbol{\zeta}_{ref}|}{\boldsymbol{\zeta}_{ref}^{max}}\right)\right) \cdot 100 \qquad (15)$$

where $\boldsymbol{\zeta}_{ref}$ is the reference response, obtained for the smallest dt. Note that a single value for ε is obtained, as the mean of the errors in surge, heave, and pitch. The computational time is normalized against the time required when the smallest dt is used. By setting an arbitrary threshold of $\varepsilon = 1\%$, a time step of 0.04s is selected. The resulting computational time, for both geometries and all waves, is Tabulated in Table III. The algorithm is implemented in *ad hoc* Matlab code, and run on a single processor of a standard computer (Dell, Precision T5810, Intel® Xeon® CPU E5-1620v3 @ 3.50GHz; RAM:16GB). Table III tabulates the normalized computational time, defined as the ratio between run-time and simulation time, so that the real-time computation requirement translates into a normalized time less or equal than one. Overall, the NLFK model computes from 4.6 to 13.2 times slower than real time. Considering that this implementation was not optimized for computational speed, and that Matlab is inherently 1 to 2 orders of magnitude slower than lower level coding languages, such as C or Fortran [12], real-time computation is potentially an easily achievable goal.

Analysing Table III in more detail, it can be remarked that G_2 is more time-demanding than G_1. On the one hand, G_1 can be described by 2 geometrical sections (one hemisphere and one cylinder), plus the top disk in the event that the wave overtops the floater. On the other hand, G_2 requires considering two cylinders (external surface and moonpool), one bottom disk, and potentially the top disk in case of overtopping waves. Since the number of FK integrals is proportional to the number of different geometrical sections composing the device, the normalized time for G_2 is larger than the one for G_1. Likewise, the computation is slower with the largest wave (3BT3), likely because overtopping events happen for a longer time.

TABLE III
Normalized computational time (run-time over simulation time), using the nonlinear Froude-Krylov model.

	G_1	G_2
1BT2	4.6	12.5
2BT2	4.6	13.1
3BT2	4.7	13.2

However, note that the computational time required by the nonlinear FK model also depends on the number of frequency components which, assuming a constant fundamental frequency (depending on the simulated time window), depends on the cut-off frequency (ω_c). Although the energy content at high frequency is rather small, and usually negligible for accurately reproducing ordinary panchromatic waves, it is significant in the case of focused waves. In fact, phases are such that all frequency components have a constructive interaction at the focused location and combine to create the peak. This is one of the reasons why focused waves are particularly challenging to simulate with a nonlinear FK approach, especially for validation purposes, where the ability to replicate the incoming wave is essential. Figure 8 shows how the cut-off frequency, hence the number of frequency components (n_ω), affects the computational time (t_n) and the ability to replicate the peak of the focused wave (η_{max}). The consequent error in reproducing the peak (ε_η) and the computational time are normalized against the case with higher ω_c.

The impact of ε_η on the response of the device is shown in Fig. 9, for the example of geometry G_2, using the percentage error as in (15). It can be remarked that the surge degree of freedom is the most affected, while heave and pitch are less sensitive to the η_{max}.

Based on Figures 8 and 9, the chosen cut-off frequency for the analysis is 14 rad·s^{-1}. The resulting time traces are shown in Figs. 10 and 11, for geometry G_1 and G_2, respectively. The most worthwhile remark is the clear and significant drift of both geometries in surge, especially with the larger wave 3BT2. Drift is a purely nonlinear phenomenon, hence unnoticed by linear hydrodynamic models. In particular, nonlinearities are significant at larger and steeper waves.

Finally, it is important to highlight that no viscous effect has been included in the equation of motion (3). While this is a reasonable assumption for the smooth geometry G_1, sharp edges of geometry G_2 are likely to generate vortex shedding, hence viscous losses. However, for this study it was not possible to perform an drag identification test to estimate the drag coefficient. A sensitivity analysis is performed instead, in order to evaluate the effect of viscous effects on the floater response.

The most common way to include viscous drag

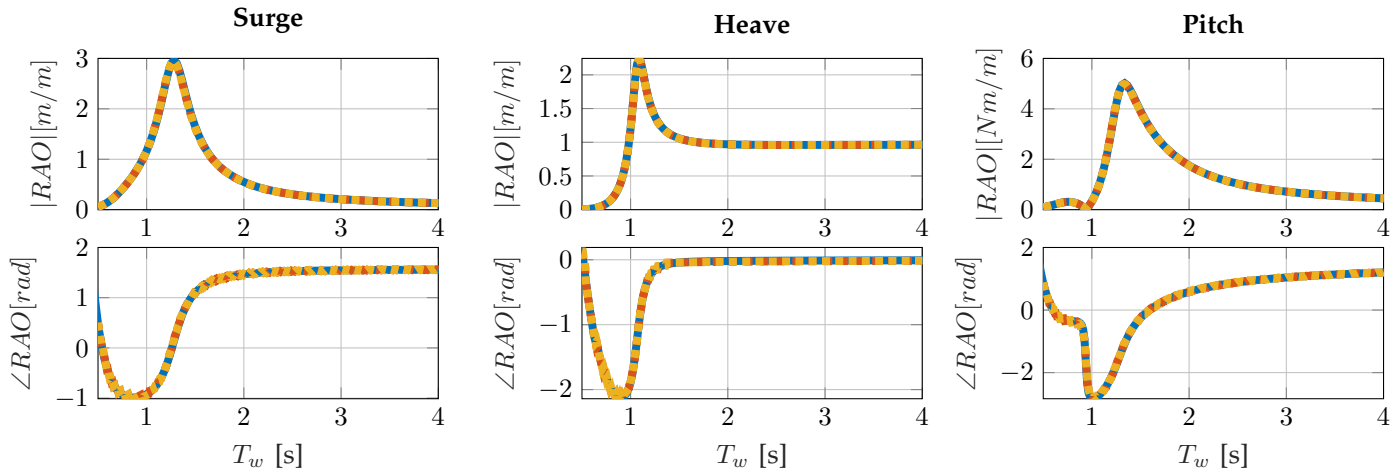

Fig. 5. Response amplitude operator for geometry G_1, computed in linear conditions (1mm wave height and linear moorings) in the time domain using a fully-linear (▪▪▪) and a nonlinear (▪▪▪) model, successfully compared to frequency domain calculations (▬).

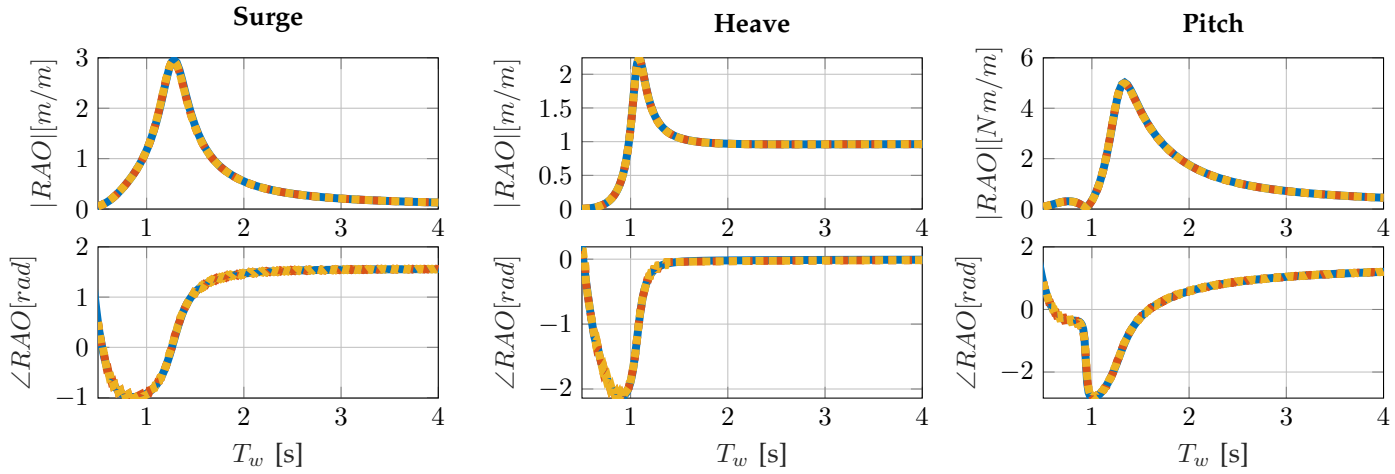

Fig. 6. Response amplitude operator for geometry G_2, computed in linear conditions (1mm wave height and linear moorings) in the time domain using a fully-linear (▪▪▪) and a nonlinear (▪▪▪) model, successfully compared to frequency domain calculations (▬).

effects in partially-nonlinear mathematical models for WECs is through a Morison-like term [20]. Since the main source of viscous losses is the vertical motion, only the heave component of the viscous force is modelled, as:

$$f_{vis} = -\frac{1}{2}\rho\, C_d A_d \left|\dot{\hat{z}} - V_0\right| (\dot{z} - V_0), \tag{16}$$

where ρ is the water density, C_d the drag coefficient, A_d projected area perpendicular to the flow, and V_0 the undisturbed flow velocity. Figure 12 shows the response of geometry G_2, applying the viscous force in (16) to a fully-linear model and to the nonlinear model, varying the drag coefficient from 0 to 1.4.

In the fully-linear model, the viscous force in the vertical direction affects the heave response only. In fact, there is no linear hydrodynamic coupling between heave and surge/pitch, and the only coupling provided by the mooring line is weak, since the relative angle between the mooring line and the axis of the floater is negligible.

On the contrary, in the nonlinear model, it is clear that the viscous force in heave significantly affects all degrees of freedom, especially surge, since nonlinear FK forces and nonlinear kinematics provide a strong nonlinear coupling between all modes of motion. Consequently, viscous drag significantly reduces drift forces, so that the maximum surge position is smaller as C_d increases, which has important consequences for the design of mooring lines. Furthermore, considering the heave response, it can be remarked that the viscous force acts as a low pass filter in both models, smoothing out higher frequency response after the peak.

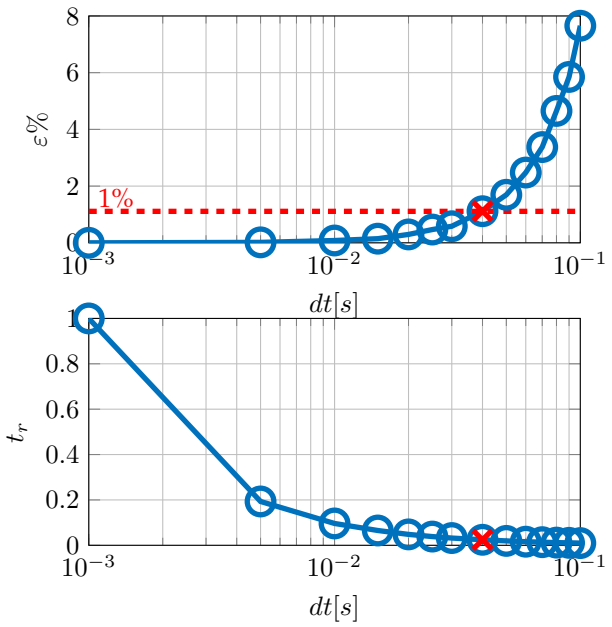

Fig. 7. Normalized computational time t_r and mean percentage error ε, defined as in (15), for different time steps dt, for geometry G_1 and wave 3BT2.

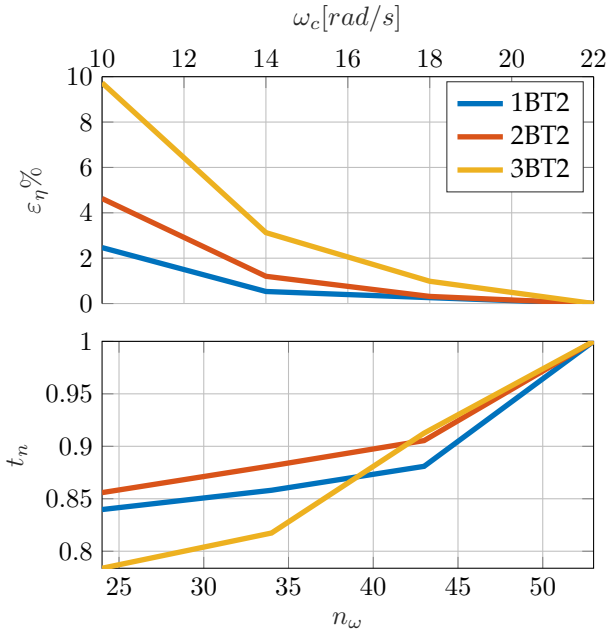

Fig. 8. Relative error on the peak of the focused wave surface elevation (ε_η) and normalized computational time (t_n) with respect to the cut-off frequency (ω_c) and number of frequency components (n_ω). Note that there is a one-to-one relationship between ω_c and n_ω. The case with maximum ω_c is used for the normalization.

V. Conclusion

The current stage of development of hydrodynamic models for wave energy applications highlights the urgent need for standardization of modelling techniques and evaluation/comparison metrics, which are essential for developing more confidence and effectiveness of the design process. The CCP-WSI project aims to provide common experimental data to different institutions, in order to implement and compare various modelling techniques. In general, the choice of the model is guided by the particular requirements of the intended application, especially the accuracy/computational time balance. This paper proposes a model which achieves a medium-high level of a accuracy, but keeps the run-time close to real-time. Therefore, nonlinear kinematics and nonlinear Froude-Krylov force calculations are implemented, exploiting the axisymmetric shape of the floaters to enhance the computational performance of the model. Data provided by the CCP-WSI project will be useful for validating the model with experimental data. Here the model is used to discuss issues related to using a partially-nonlinear model for focused waves as opposed to real panchromatic waves, and for validation as opposed to simulation. Furthermore, some nonlinear effects are shown, especially drift, nonlinear coupling between different degrees of freedom, and sensitivity to viscous effects.

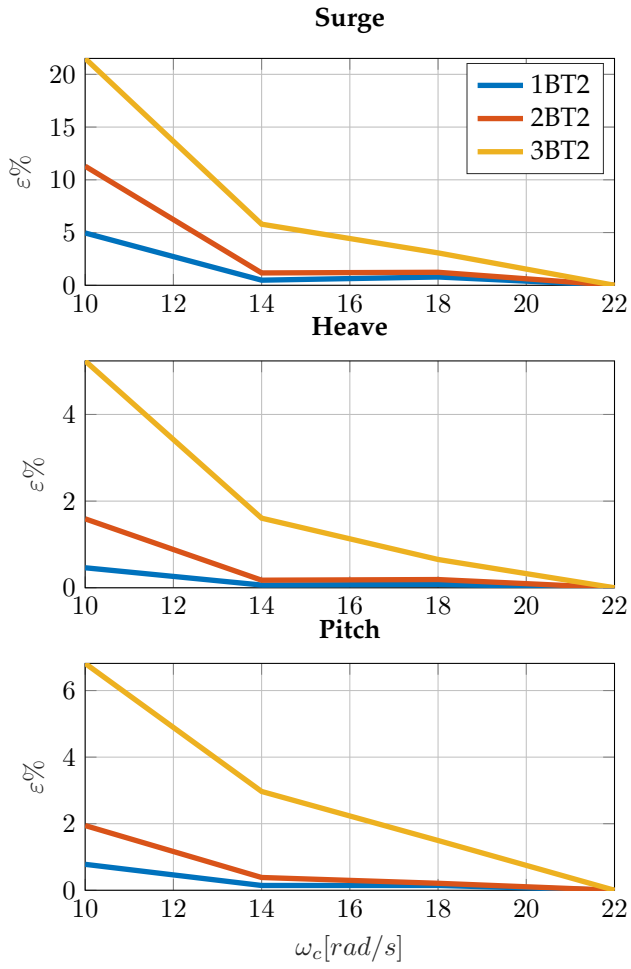

Fig. 9. Error in the surge, heave, and pitch response of geometry G_2, depending on the adopted cut-off frequency ω_c, due to the relative error ε_η, shown in Fig. 8.

References

[1] G. Giorgi and J. V. Ringwood, "Computationally efficient nonlinear Froude–Krylov force calculations for heaving axisymmetric wave energy point absorbers," *Journal of Ocean Engineering and Marine Energy*, vol. 3, no. 1, pp. 21–33, 2017.

[2] J. V. Ringwood, A. Merigaud, N. Faedo, and F. Fusco, "Wave Energy Control Systems: Robustness Issues," in *Proceedinds of the IFAC Conference on control Aplications in Marine Systems, Robotics, and Vehicles*, 2018.

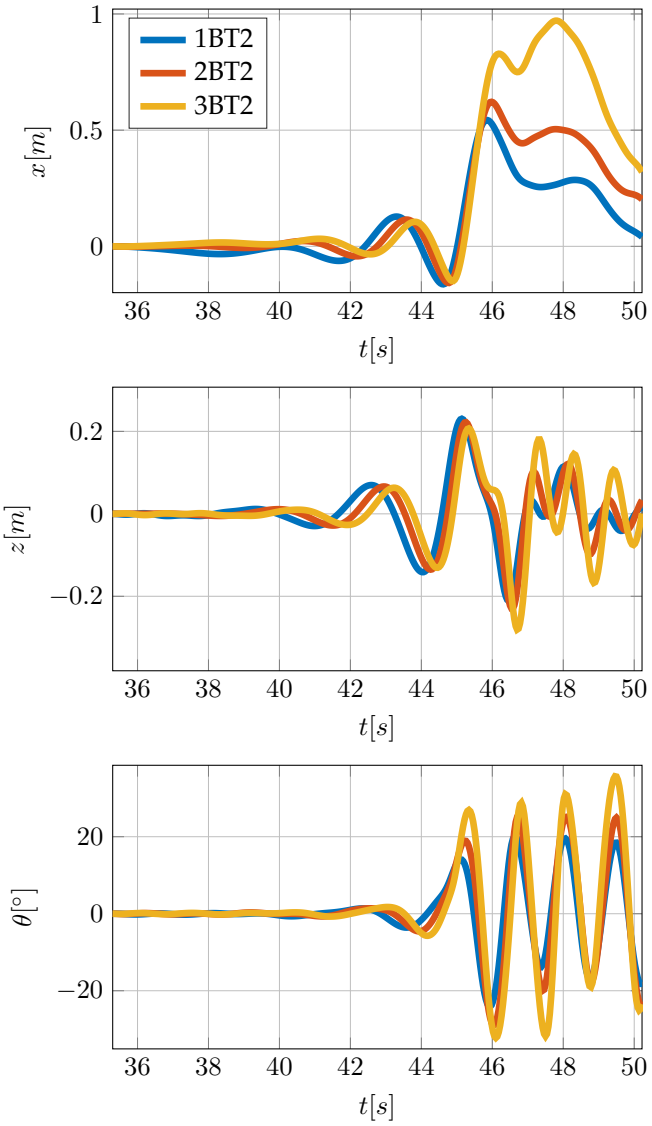

Fig. 10. Response of geometry G_1 in surge (x), heave (z), and pitch (θ).

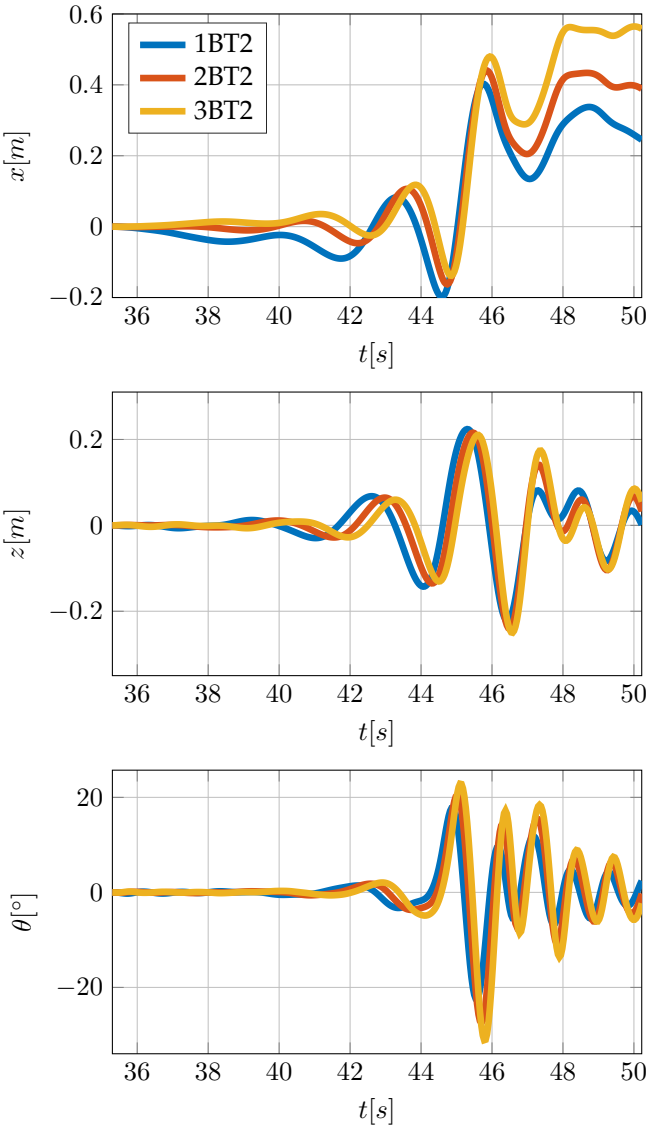

Fig. 11. Response of geometry G_2 in surge (x), heave (z), and pitch (θ).

[3] S. H. Salter, "Wave Power," *Nature*, vol. 249, no. 720-724, pp. 720–724, jun 1974. [Online]. Available: http://www.nature.com/articles/249720a0

[4] M. Penalba, G. Giorgi, and J. V. Ringwood, "Mathematical modelling of wave energy converters: a review of nonlinear approaches," *Renewable and Sustainable Energy Reviews*, vol. 78, pp. 1188–1207, 2017. [Online]. Available: http://www.eeng.nuim.ie/coer/wp-content/uploads/2017/05/J270MRGG-3.pdf

[5] M. Penalba, A. Mérigaud, J. C. Gilloteaux, and J. V. Ringwood, "Influence of nonlinear FroudeKrylov forces on the performance of two wave energy points absorbers," *Journal of Ocean Engineering and Marine Energy*, vol. 3, no. 3, pp. 209–220, 2017.

[6] A. H. Clément and P. Ferrant, "Nonlinear Water Waves: IUTAM Symposium, Tokyo Japan, August 25–28, 1987," K. Horikawa and H. Maruo, Eds. Berlin, Heidelberg: Springer Berlin Heidelberg, 1988, ch. Superharmo, pp. 423–433.

[7] G. Giorgi and J. V. Ringwood, "Relevance of pressure field accuracy for nonlinear FroudeKrylov force calculations for wave energy devices," *Journal of Ocean Engineering and Marine Energy*, vol. 4, no. 1, pp. 57–71, 2018.

[8] ——, "Comparing nonlinear hydrodynamic forces in heaving point absorbers and oscillating wave surge converters," *Journal of Ocean Engineering and Marine Energy*, vol. 4, no. 1, pp. 25–35, 2018.

[9] ——, "Froude-Krylov and Viscous Drag Representations in Nonlinear Wave Energy Devices Models in the Computation/Fidelity Continuum," *Ocean Engineering*, vol. 141, pp. 164–175, 2017.

[10] CCP-WSI, "Wave Structure Interaction Computation and Experiment Roadmap," Tech. Rep., 2016.

[11] P. B. Garcia-Rosa, R. Costello, F. Dias, and J. V. Ringwood, "Hydrodynamic Modelling Competition: Overview and approaches," in *Proceedings of the ASME 2015 34th International Conference on Ocean, Offshore and Arctic Engineering*, 2015.

[12] F. F. Wendt, Y.-H. Yu, K. Nielsen, K. Ruehl, T. Bunnik, I. Touzon, B. W. Nam, J. S. Kim, K.-H. Kim, and C. E. Janson, "International Energy Agency Ocean Energy Systems Task 10 Wave Energy Converter Modeling Verification and Validation," in *Proceedings of the 12th European Wave and Tidal Energy Conference*. Cork: Technical Committee of the European Wave and Tidal Energy Conference, 2017.

[13] Y. S. B. S. M. T. G. D. M. Q. M. P.-H. E.-K. A. P. E. C. L. Q. W. J. X. Z. S. V. S. T. Z. Y. L. Q. W. D. C. G. C. H. Q. L. M. Z. M. C. C. D. G. I. J. H. V. V. D. S. H. P. B. E. S. D. C. Q. Z. J. G. D. Ransley, E., "A blind comparative study of focused wave interactions with a fixed fpso-like structure (ccp-wsi blind test series 1)," *International Journal of Offshore and Polar Engineering (in press)*, 2019.

[14] T. I. Fossen, *Handbook of marine craft hydrodynamics and motion control*. John Wiley & Sons, 2011.

[15] G. Giorgi and J. V. Ringwood, "Analytical representation of nonlinear Froude-Krylov forces for 3-DoF point absorbing wave energy devices," *Ocean Engineering*, vol. 164, no. 2018, pp. 749–759, 2018.

[16] N. Faedo, Y. Peña-Sanchez, and J. V. Ringwood, "Finite-Order Hydrodynamic Model Determination for Wave Energy Applications Using Moment-Matching," *Ocean Engineering*, vol. 163, pp. 251–263, 2018.

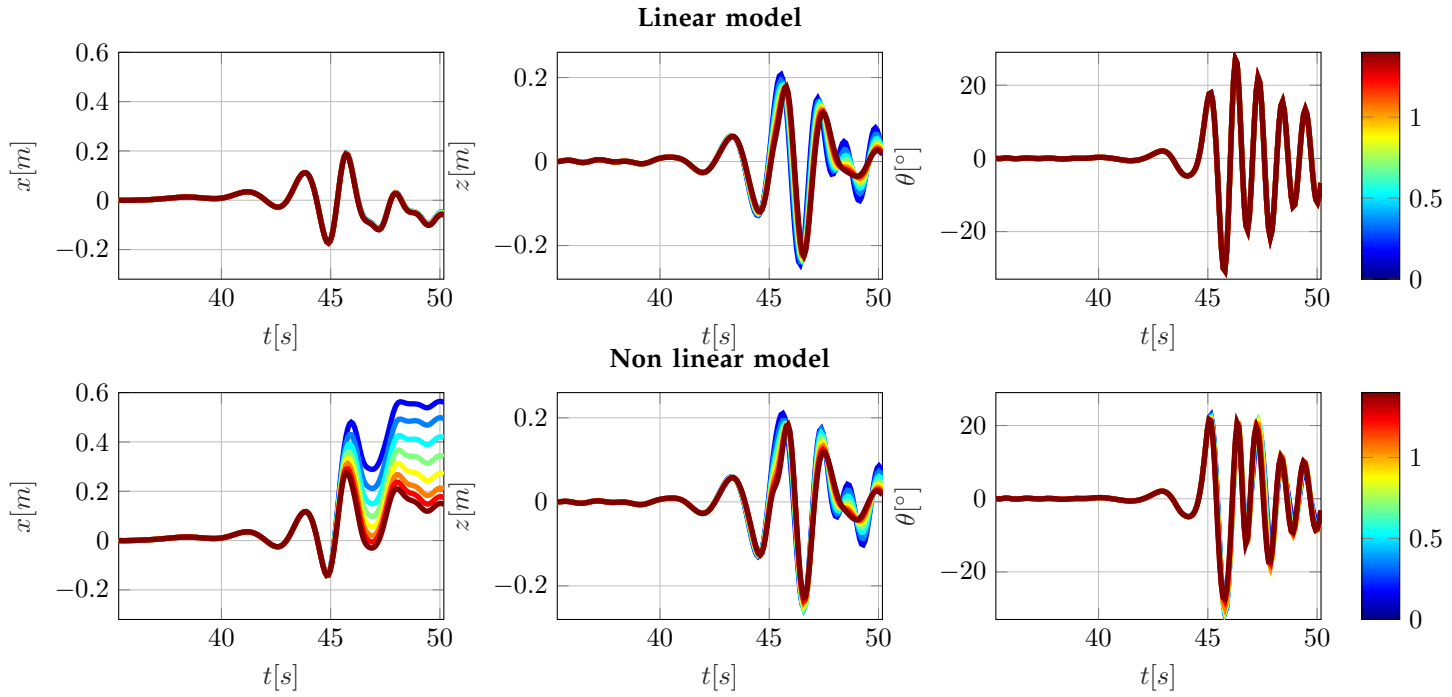

Fig. 12. Response of geometry G_2 to wave 3BT2, applying the viscous force in (16) to a fully-linear model and to the nonlinear model, varying the drag coefficient C_d from 0 to 1.4 (shown in the colorbar).

[17] J.-C. Gilloteaux, "Mouvements de grande amplitude d'un corps flottant en fluide parfait. Application á la recuperation de l'energie des vagues," Ph.D. dissertation, Ecole Centrale de Nantes-ECN, 2007.

[18] G. Giorgi and J. V. Ringwood, "Articulating Parametric Nonlinearities in Computationally Efficient Hydrodynamic Models," in *Proceedings of the 11th IFAC Conferecne on Control Applications in Marine Systems, Robotics, and Vehicles*, Opatija, 2018.

[19] D. Z. Ning, J. Zang, S. X. Liu, R. Eatock Taylor, B. Teng, and P. H. Taylor, "Free-surface evolution and wave kinematics for nonlinear uni-directional focused wave groups," *Ocean Engineering*, vol. 36, no. 15-16, pp. 1226–1243, 2009. [Online]. Available: http://dx.doi.org/10.1016/j.oceaneng.2009.07.011

[20] M. A. Bhinder, A. Babarit, L. Gentaz, and P. Ferrant, "Assessment of viscous damping via 3d-cfd modelling of a floating wave energy device," in *Proceedings of the 9th European Wave and Tidal Energy Conference*, Southampton, 2011.